

Optical tomography for biomedical applications by digital interference holography

M C Potcoava and M K Kim

Department of Physics, University of South Florida, Tampa, FL 33620, USA

E-mail: mpotcoav@mail.usf.edu and mkkim@cas.usf.edu

Received 10 September 2007, in final form 20 February 2008

Published 23 May 2008

Online at stacks.iop.org/MST/19/074010

Abstract

We present results of imaging experiments using digital interference holography (DIH). Calibration experiments using a resolution target demonstrate an improvement of signal-to-noise ratio (SNR) with increasing number of holograms consistent with theoretical prediction. Imaging experiments on retinal tissue reveal the topography of blood vessels as well as the optical thickness profile of the retinal layer. The SNR of tissue images is comparable to that of the resolution target, implying that the imaging system is operating close to theoretical optimum.

Keywords: digital interference holography, angular spectrum, wavelength scanning, optical design, biological tissues

1. Introduction

One of the important challenges for biomedical optics is noninvasive three-dimensional imaging, and various techniques have been proposed and are available. For example, confocal scanning microscopy provides high-resolution sectioning and in-focus images of a specimen. However, it is intrinsically limited in frame rate due to serial acquisition of the image pixels. Ophthalmic imaging applications of laser scanning *in vivo* confocal microscopy have been recently reviewed [1]. Another technique, optical coherence tomography (OCT), is a scanning microscopic imaging technique with micrometer scale axial and lateral resolutions, based on low coherence or white light interferometry to coherently gate the backscattered signal from different depths in the object [2, 3]. Swept-source optical coherence tomography is a significant improvement over the time-domain OCT [4–6], in terms of the acquisition speed and signal-to-noise ratio (SNR). A related technique of wavelength scanning interferometry uses the phase of the interference signal, between the reference light and the object light which varies in the time while the wavelength of a source is swept over a range. A height resolution of about 3 μm has been reported using a Ti:sapphire laser with a wavelength scanning range of about 100 nm [7, 8]. The technique of structured illumination

microscopy provides wide-field depth-resolved imaging with no requirement for time-of-flight gated detection [9].

The principle of holography was introduced by Gabor [10] in 1948, as a technique where wavefronts from an object were recorded and reconstructed in such a way that not only the amplitude but also the phase of the wave field was recovered. In 1967, Goodman demonstrated the feasibility of numerical reconstruction of a holographic image using a densitometer-scanned holographic plate [11]. Schnars and Jüptner, in 1994, were the first to use a CCD camera connected to a computer as the input, completely eliminating the photochemical process, in what is now referred to as digital holography [12–14]. Various useful and special techniques have been developed to enhance the capabilities and to extend the range of applications. Phase-shifting digital holography allows elimination of zero-order and twin-image components even in an on-axis arrangement [15–17]. Optical scanning holography can generate holographic images of fluorescence [18]. Three-channel color digital holography has been demonstrated [19]. Application of digital holography in microscopy is especially important, because of the extremely narrow depth of focus of high-magnification systems [20, 21]. Numerical focusing of holographic images can be accomplished from a single exposed hologram. Direct accessibility of phase information can be utilized for the numerical correction of various

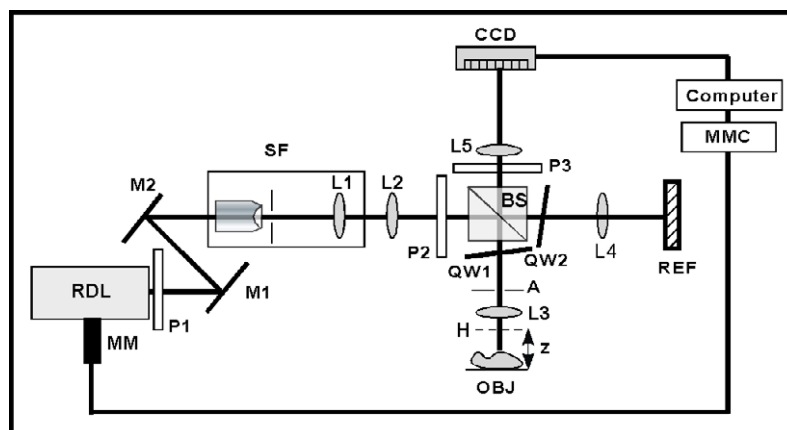


Figure 1. DIH optical apparatus. RDL: ring dye laser; M_i : mirrors; SF: spatial filter and expander; L_i : lenses; P_i : polarizers; BS: polarizing beamsplitter; QW i : quarter waveplates; A: aperture; H: hologram plane; OBJ: object; REF: reference mirror; MM: motorized micrometer; MMC: controller for MM.

aberrations of the optical system, such as field curvature and anamorphism [22]. Digital holography has been particularly useful in metrology, deformation measurement and vibrational analysis [23–25]. Microscopic imaging by digital holography has been applied to the imaging of microstructures and biological systems [23, 26, 27]. We have developed digital interference holography for optical tomographic imaging [28–33] as well as multiwavelength quantitative phase contrast digital holography for high resolution microscopy [34–37].

In the last few years, the scanning wavelength technique in various setups has been adopted by researchers for three-dimensional imaging of microscopic and submicroscopic samples. When digital holography is combined with optical coherence tomography, a series of holograms are obtained by varying the reference path length [38]. A new tomographic method that combines the principle of DIH with spectral interferometry has been developed using a broadband source and a line-scan camera in a fiber-based setup [39]. Sub-wavelength resolution phase microscopy has been demonstrated [40] using a full-field swept-source for surface profiling. Nanoscale cell dynamics was reported using cross-sectional spectral domain phase microscopy (SDPM) with the lateral resolution better than $2.2 \mu\text{m}$ and the axial resolution of about $3 \mu\text{m}$ [41]. A spectral shaping technique for DIH is seen to suppress the sidelobes of the amplitude modulation function and to improve the performance of the tomographic system [42]. Submicrometer resolution of DIH has been demonstrated [43].

Another optical tomographic technique, applied widely for determination of the refractive index [44–49], is based on acquiring multiple interferograms while the sample rotates. The reconstruction of the phase distribution is performed using the filtered back-projection algorithm. Then the phase distribution is scaled to refractive index values. The refractive index distribution reveals information about the cellular internal structure of a transparent or semitransparent specimen.

In this paper, we use computer and holographic techniques with digital interference holography (DIH) to accurately and

consistently identify and quantify different object structures with μm resolution. This technique is based on an original numerical method [28], where a three-dimensional microscopic structure of a specimen can be reconstructed by succession of holograms recorded using an extended group of scanned wavelengths. The paper is organized as follows: section 2 describes the design of the apparatus and the scanning characteristics of the light source; section 3 reviews current reconstruction algorithms and emphasizes the angular spectrum method; the digital interference holography technique is reviewed in section 4; section 5 presents animal tissue reconstructed amplitude images; finally, conclusions are presented in section 6.

2. DIH apparatus

The basic configuration of the apparatus is a Michelson interferometer, figure 1. The light source is a Coherent 699 ring dye laser, pumped by Millennia V diode pumped solid-state laser, tunable over a range of 565–615 nm with an output power of up to 500 mW. The laser output is spatial filtered and collimated. The focusing lens L2 focuses the laser on the back focus of the objective lens L3, so that the object is illuminated by a collimated beam. The lenses L3 and L5 form a microscope pair, so that the CCD acquires a magnified image of a plane H in the vicinity of the object plane. The reference mirror is an optical conjugate of the plane H through the matching objective lens L4. Then the image acquired by the CCD is equivalent to a holographic interference between a plane reference wave and the object wave that has propagated (diffracted) over a distance z from the object plane. In general, the object plane may be at an arbitrary distance z from the hologram plane H, and the object can be numerically brought back in focus by the digital holography process. But in practice, it is advantageous to keep the object plane in focus to simplify the optical alignment and to help identify the object portion being imaged, as well as minimizing potential secondary aberration effects. The polarization optics—polarizer P2, analyzer P3, quarter wave plates and polarizing beam splitter—is used to

continuously adjust the relative partition of optical power between the object and reference fields and to maximize the interference contrast. The polarizer P1 at the output of the laser is used to continuously adjust the overall power input to the interferometer. The CCD camera (Sony XC-ST50) has 780×640 pixels with a $9 \mu\text{m}$ pitch, and is digitized with an 8-bit monochrome image acquisition board (NI IMAQ PCI-1407). Slight rotations of the reference mirror and object planes enable the acquisition of an off-axis hologram. A variable aperture placed at the back focal (Fourier) plane of the objective lens L3 can be useful in controlling the angular spectrum of the object field.

2.1. The tuning characteristics of the light source

The light source used in this experiment was a dye laser pumped by a solid state laser. The wavelength tunable range of 34 nm for this experiment was between 568 nm and 602 nm. The tunable range of wavelengths determines the axial resolution of the image, while the tuning resolution or the wavelength increment determines the axial range, or the axial size of an object. The ability to distinguish axial distances of various layers of a tissue is called axial resolution, δz . This tuning parameter is obtained in the following way:

$$k = \frac{2\pi}{\lambda}, \quad \delta k = \frac{2\pi \delta \lambda}{\lambda^2}, \quad \Lambda = \frac{2\pi}{\delta k} = \frac{\lambda^2}{\delta \lambda}, \quad \delta z = \frac{\Lambda}{N}, \quad (1)$$

where λ is the center wavelength, $\delta \lambda$ is the wavelength increment, k is the wavevector, δk is the wave number increment, δz is the axial resolution and Λ is the object axial size. For example, a dye laser tunable over a 34 nm range, for 50 wavelengths, centered at 585 nm results in an axial resolution of about $\delta z = 10 \mu\text{m}$ and an axial range of $\Lambda = 500 \mu\text{m}$. The scanning process is controlled using a stepper motor that changes the birefringent filter of the laser in small increments, changing the laser wavelength when it rotates.

3. Numerical reconstruction of the hologram by the angular spectrum method

We have found that the use of the angular spectrum algorithm has a number of advantages over more commonly used Fresnel transform or Huygens convolution methods [32]. Suppose $E_0(x_0, y_0)$ represents the two-dimensional optical field at the hologram plane, then its angular spectrum is the Fourier transform

$$F(k_x, k_y; 0) = \iint E_0(x_0, y_0) \exp[-i(k_x x_0 + k_y y_0)] dx_0 dy_0, \quad (2)$$

where k_x and k_y are the spatial frequencies. The angular spectrum of an off-axis hologram contains a zero-order and a pair of first-order components, the latter corresponding to the twin holographic images. One of the first-order components in $F(k_x, k_y; 0)$ can be separated from the others with a numerical band-pass filter if the off-axis angle of the reference beam is properly adjusted. The object field can then be rewritten as the

inverse Fourier transform of the angular spectrum, properly filtered:

$$E(x_0, y_0) = \iint F(k_x, k_y; 0) \exp[i(k_x x_0 + k_y y_0)] dk_x dk_y. \quad (3)$$

The field distribution after propagation over a distance z is then

$$\begin{aligned} E(x, y; z) &= \iint F(k_x, k_y; 0) \exp[i(k_x x + k_y y + k_z z)] dk_x dk_y \\ &= F^{-1}\{F\{E_0\} \exp[ik_z z]\}, \end{aligned} \quad (4)$$

where $k_z = [k^2 - k_x^2 - k_y^2]^{1/2}$, $k = 2\pi/\lambda$ and the symbol F denotes the Fourier transform. Distinct advantages of the angular spectrum method include consistent pixel resolution, no minimum reconstruction distance and easy filtering of noise and background components. Once the angular spectrum at $z = 0$ is calculated by a Fourier transform, the field at any other z -plane can be calculated with just one more Fourier transform, whereas the Fresnel or convolution methods require two or three Fourier transforms for each value of z . Analytically, the angular spectrum method is equivalent to the Huygens convolution method, because

$$E(x, y; z) = E_0 \otimes h = F^{-1}\{F\{E_0\} \cdot F\{h\}\}, \quad (5)$$

where \otimes represents convolution, $h \propto \exp(ikr) = \exp[ik\sqrt{x^2 + y^2 + z^2}]$ is the point spread function and $F\{h\} \propto \exp(ik_z z)$ is the coherence transfer function. But the numerical calculations over a discretized finite plane H behave very differently between these methods. The Huygens method, based on the convolution of the spherical wavelets, has a minimum distance requirement to avoid aliasing of spherical wavefronts of high curvature as well as a maximum distance to be able to account for spherical wavefronts of high enough fringe frequency across the hologram plane. On the other hand, the angular spectrum method accounts for all the recorded spatial frequencies of the hologram and this spectral content of plane waves is independent of the propagation distance. A detailed comparative study of reconstruction methods in digital holography will be reported in another publication.

4. Principle of digital interference holography [28–33]

Suppose an object is illuminated by a laser beam of wavelength λ . A point r_0 on the object scatters the light into a Huygens wavelet, $A(r_0) \exp(ik|r - r_0|)$, where the object function $A(r_0)$ is proportional to the amplitude and phase of the wavelet scattered or emitted by object points, figure 2(a). For an extended object, the field at r is $E(r) \sim \int A(r_0) \exp(ik|r - r_0|) d^3 r_0$, where the integral is over the object volume. The amplitude and phase of this field at the hologram plane $z = 0$ are recorded by the hologram, as $H(x_h, y_h; \lambda)$. The holographic process is repeated using N different wavelengths, generating the holograms $H(x_h, y_h; \lambda_1), H(x_h, y_h; \lambda_2), \dots, H(x_h, y_h; \lambda_N)$. From each of the holograms, the field $E(x, y, z; \lambda)$ is calculated as a complex 3D array over the volume in the vicinity of the object, figure 2(b). Superposition of these N 3D arrays results in $\sum_k \int A(r_0) \exp(ik|r - r_0|) d^3 r_0 \sim \int A(r_0) \delta(r - r_0) d^3 r_0 \sim A(r)$. That is, for a large enough number of wavelengths,

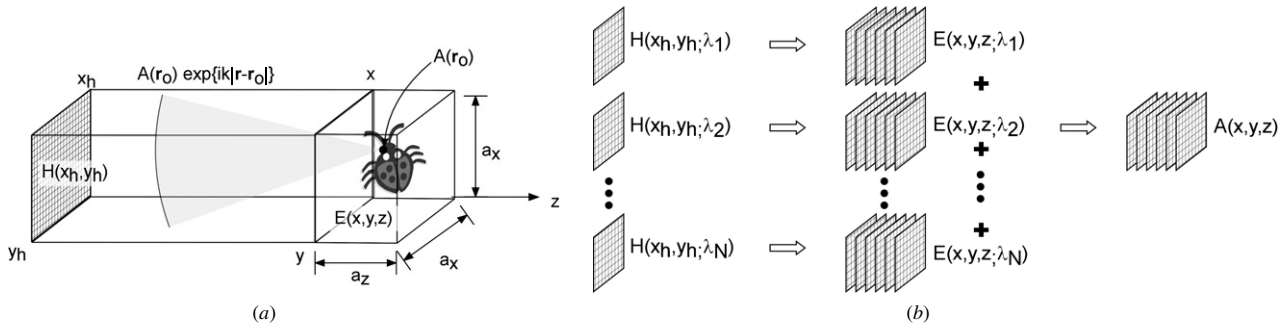


Figure 2. (a) Geometry and (b) process of DIH. H: hologram; E: optical field in the object volume; A: object function. See the text for more details.

the resultant field is proportional to the field at the object and is nonzero only at the object points. In practice, if one uses a finite number N of wavelengths, with uniform increment $\Delta(1/\lambda)$ of the inverse wavelengths, then the object image $A(r)$ repeats itself (other than the diffraction/defocusing effect of propagation) at a beat wavelength $\Lambda = [\Delta(1/\lambda)]^{-1}$, with the axial resolution $\delta = \Lambda/N$. By use of appropriate values of $\Delta(1/\lambda)$ and N , the beat wavelength Λ can be matched to the axial range of the object and δ to the desired level of axial resolution.

Addition of a series of N cosines or imaginary exponentials yields $S = \frac{1}{N} \sum_{n=1}^N \exp(in\delta kz)$, so that $|S|^2 = \frac{\sin^2(N\pi z/\Lambda)}{N^2 \sin^2(\pi z/\Lambda)}$, where $\delta k = 2\pi/\Lambda$. The SNR of the peaks at $z = 0, \Lambda, \dots$ grows proportional to N^2 , while the width of the peak narrows as $\delta \sim \Lambda/N$. This behavior of the SNR and resolution is achieved only if all the amplitudes and phases of cosines are identical. Each hologram captured by the camera is normalized by the 2D average of each hologram to compensate for the laser power variation across the tuning range.

$$H_{\text{norm}}(x_h, y_h; \lambda_n) = \frac{H(x_h, y_h; \lambda_n)}{\sum_{x_h, y_h} H(x_h, y_h; \lambda_n)/N_x N_y}. \quad (6)$$

The phase calculated by digital holography is given by $\varphi = kZ = 2\pi Z/\lambda$, where Z is the distance of an object point relative to the position of the reference mirror and λ is the wavelength of the laser. Uncertainty in k or Z leads to a phase error, which needs to be corrected for. For example, from each hologram $H(\lambda_n)$, a 2D phase profile is calculated $\varphi_n(x, y) = \text{phase}\{E(x, y, z; \lambda_n)\}$ at a suitable value of z that corresponds to a location near the object. Then calculate the difference profiles $\delta\varphi_n(x, y) = \varphi_n(x, y) - \varphi_{n-1}(x, y) = \delta k \cdot Z(x, y)$, where $Z(x, y)$ is the Z -profile of the object being imaged. If δk s are perfectly equally spaced between holograms, then all $\delta\varphi_n$ s for various n s should be identical. Otherwise, the uncertainties introduce the phase error ε_n , so that the measured phase differences are $\delta\varphi'_n(x, y) = (\delta k + \Delta k) \cdot Z = \delta\varphi_n(x, y) + \varepsilon_n$, where Δk is the deviation from the nominally constant δk . The trick is to determine the series $\varepsilon_2, \varepsilon_3, \dots, \varepsilon_n$ that makes $\delta\varphi_2, \delta\varphi_3, \dots, \delta\varphi_n$ as identical as possible. To find ε_2 , for example, take the difference $\delta\varphi'_3 - \delta\varphi'_2$ plus a value of ε_2 , modulo 2π , and take the average over (x, y) . Do this for a number of ε_2 values in the range of 0 to 2π until the one is found that minimizes $\delta\varphi'_3 - \delta\varphi'_2$. This procedure works

best if $Z(x, y)$ is a well-defined 2D function. With diffuse or multilayered objects, one assumes that the phase is mostly determined by the top surface of a tissue, for example. With the retinal sample objects presented below, this seems to be the case, whereas in imaging experiments with more diffuse texture, such as mouse skin, the resultant images are noisier and of lesser contrast. It is also noted that the error $\varepsilon_n = \Delta k \cdot Z$ is larger if Z is larger, so that it is advantageous to keep Z as small as possible, that is, to keep the reference mirror position to match the object position as closely as possible.

5. Results

5.1. Resolution target

We used a US Air Force resolution target to calibrate the system. The $1040 \times 1040 \mu\text{m}^2$, 256×256 pixel area selected in figure 3(a) shows group 2, elements 3 and 4 as well as group 4 elements 2 through 6. The smallest visible element, group 4 element 6, has a $17.54 \mu\text{m}$ width. The reconstruction distance z , representing the distance from the object to the hologram plane is $643.56 \mu\text{m}$. The complex field of the resolution target is computed separately for 50 wavelengths by numerical diffraction using the angular spectrum method, which gives an axial range of $\Lambda = 500 \mu\text{m}$ and axial resolution of $\delta z = 10 \mu\text{m}$. All 3D electric fields are added together to obtain a 3D volume structure of the object being imaged. Cross-sections of the volume can be taken in the x, y and z planes. Cross-sectional images in the $y-z$ planes (figure 3(b)) and $x-z$ planes (figure 3(c)) are shown below.

The resolution target is an object without internal structure and the reflection of the laser beam takes place at the surface of the resolution target. A piece of clear tape is placed on top of the resolution target to provide a second surface for demonstration of tomographic imaging. The first layer $s1$ in figures 3(b) and (c) is the reflection that comes from the chromium-coated glass surface. The second layer $s2$ is the reflection from the attached tape surface. We have tested the improvement of SNR with increasing number of holograms N . As described above, the SNR is expected to grow as N^2 . As seen in figure 4, the four-fold increase in N from 100 to 400 lowers the noise from -30 dB to about -45 dB, which is consistent with $10 \cdot \log 16 = 12$ dB. This data set is without the clear tape attachment.

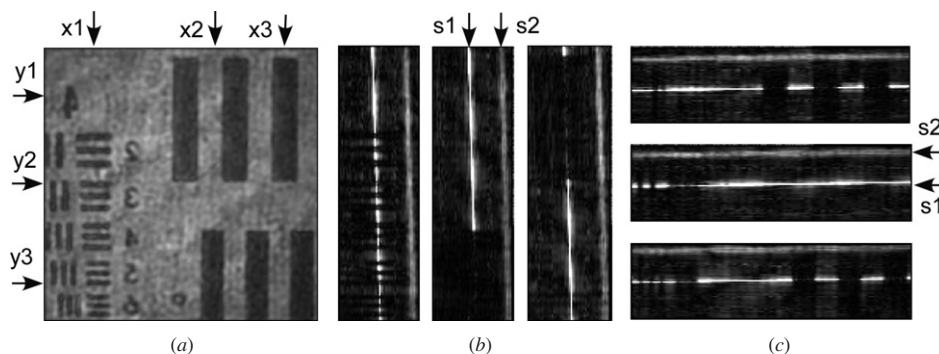


Figure 3. The reconstructed volume of the resolution target: (a) x - y cross-section, $1040 \times 1040 \mu\text{m}^2$. (b) y - z cross sections at various x values, $500 \times 1040 \mu\text{m}^2$, from left to right, x_1 , x_2 and x_3 . (c) x - z cross sections at various y values, $1040 \times 500 \mu\text{m}^2$, from top to bottom, y_1 , y_2 and y_3 . s_1 is the chromium-coated glass surface and s_2 is the surface of clear tape.

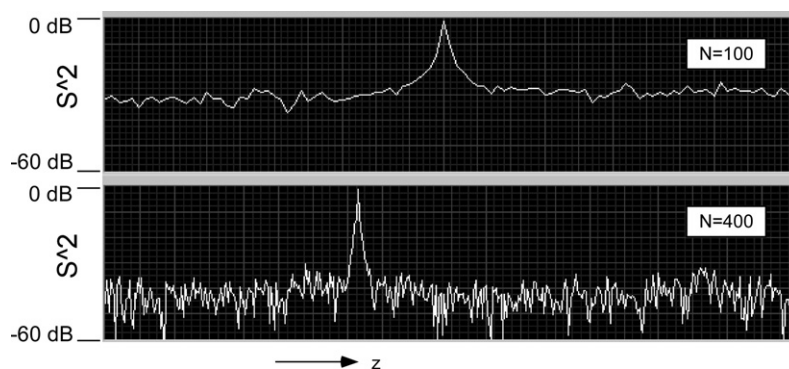


Figure 4. Improvement of SNR with number of holograms N . The peak in each semi-log graph represents the surface of the resolution target. As N increases four-fold the SNR increases by 12 dB, as expected.

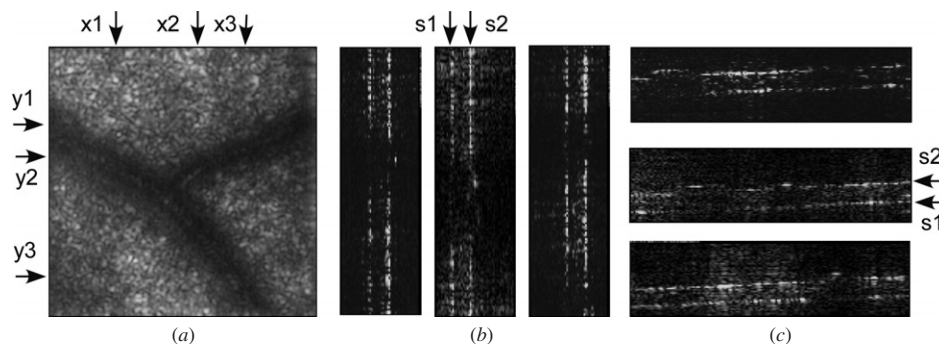


Figure 5. The reconstructed volume of the retina with blood vessels: (a) x - y *en face* image, $670 \times 670 \mu\text{m}^2$; (b) from left to right, z - y cross-sections along x_1 , x_2 and x_3 , $500 \times 670 \mu\text{m}^2$; (c) from top to bottom, x - z cross-sections along y_1 , y_2 and y_3 , $670 \times 500 \mu\text{m}^2$. s_1 is the choroidal surface and s_2 is the retinal surface.

5.2. Biological samples: pig retina

In the following, we present a few examples of tomographic imaging of biological specimens using digital interference holography. Figures 5 and 6 are images of a porcine eye tissue provided by the Ophthalmology Department at the USF. It was preserved in formaldehyde, refrigerated and a piece of the sclera, with retinal tissue attached, was cut out for imaging. The holographic image acquisition and computation of the optical field are carried out for each of 50 wavelengths in the range from 565 nm to 602 nm. Superposition of images, in

DIH processes described above, reveals the principal features of the retinal anatomy. The imaged surface areas are $0.67 \times 0.67 \text{ mm}^2$ for figure 5 and $1.04 \times 1.04 \text{ mm}^2$ for figure 6. The axial range $\Lambda = 500 \mu\text{m}$ and axial resolution $\delta z = 10 \mu\text{m}$ for both image sets. The measured SNR for these images was about 45–55 dB.

In figure 5, the images reveal convex surfaces of blood vessels, as well as about $150 \mu\text{m}$ thick layer of retina, s_2 , on top of the choroidal surface, s_1 . The blood vessels in figure 5 were apparently fixed with blood in them, while in figure 6,

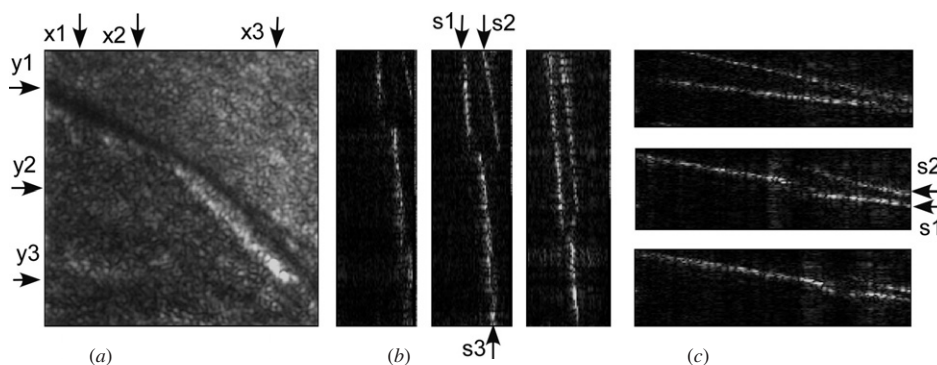


Figure 6. The reconstructed volume of torn retina on choroid: (a) x - y *en face* image, $1040 \times 1040 \mu\text{m}^2$; (b) from left to right, y - z cross-sections along x_1 , x_2 , and x_3 , $500 \times 1040 \mu\text{m}^2$; (c) from top to bottom, x - z cross sections along y_1 , y_2 and y_3 , $1040 \times 500 \mu\text{m}^2$. s_1 and s_3 are the choroidal surfaces and s_2 is the retinal surface.

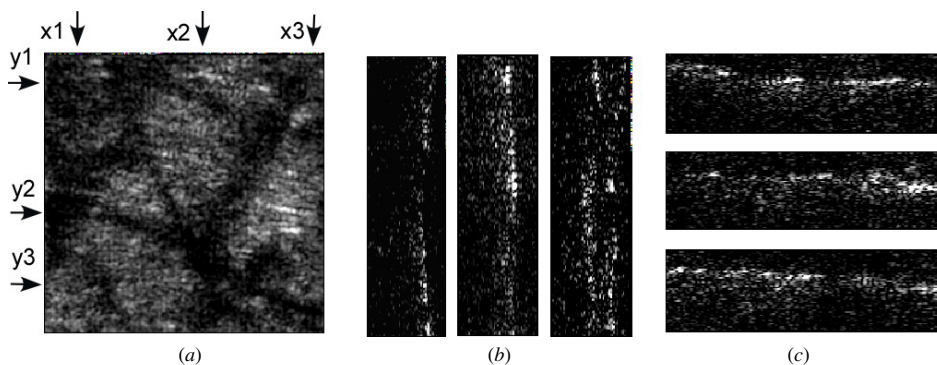


Figure 7. The reconstructed volume of mouse skin: (a) x - y *en face* image, $670 \times 670 \mu\text{m}^2$; (b) from left to right, y - z cross-sections along x_1 , x_2 and x_3 , $500 \times 670 \mu\text{m}^2$; (c) from top to bottom, x - z cross sections along y_1 , y_2 and y_3 , $670 \times 500 \mu\text{m}^2$.

the preparation and handling of the tissue sample resulted in tearing of some of the retinal tissue. Thus, the upper right half of figure 6 has intact retinal tissue, while the lower left half is missing the retinal layer and the choroidal surface is exposed. In figure 6(b), the boundary marked ‘ s_3 ’ is the bare choroidal surface, while the surface ‘ s_1 ’ is the choroidal surface seen through the retinal surface ‘ s_2 ’. The index of refraction of the retinal layer causes the choroidal surface to appear at a different depth compared to the bare surface, causing the break in the outline of the choroidal surface in figures 6(f) and (g). In fact, it is possible to estimate the index of the retinal layer from the change in apparent depth of choroidal surface, and it is consistent with the expected value in the range of 1.35–1.40. Figure 7 is the tomographic image data on a mouse skin tissue. One can discern the uppermost layer of epidermis (stratum corneum) as a distinct high reflectivity layer, while the rest of the dermis appears as a region of diffuse scattering. SNR is lower than the retina images because of the lower reflectivity of the tissue sample and the more diffuse nature of the tissue.

6. Conclusion

We have presented results of imaging experiments using digital interference holography. Calibration experiments using the resolution target demonstrate improvement of SNR with

increasing number of holograms consistent with theoretical prediction. Imaging experiments on retinal tissue reveal the topography of blood vessels as well as the optical thickness profile of the retinal layer. The SNR of tissue images is comparable to that of the resolution target, implying that the imaging system operates close to theoretical optimum. Further improvement in SNR may be achieved if the hologram number N is increased further. At this point, however, imperfection in the phase matching scheme seems to limit such improvement. We are developing a modification of the hologram exposure method so that the holograms are taken at equal intervals of wave vectors, not wavelengths, as well as automatically minimizing the reference-object distance difference by a simple interferometric tracking and feedback. This method could be applied in ophthalmology as a noninvasive, high speed imaging tool to image the retinal and choroidal substructures and will have significant applications in a variety of retinal disorders, especially macular degeneration, diabetic retinopathy and glaucoma.

Acknowledgments

The authors thank Dr Hilbelink and Dr Margo of USF School of Medicine for providing the tissue samples.

References

- [1] Patel D V and McGhee C N 2007 Contemporary *in vivo* confocal microscopy of the living human cornea using white light and laser scanning techniques: a major review *Clin. Exp. Ophthalmol.* **35** 71–88
- [2] Huang D *et al* 1991 Optical coherence tomography *Science* **254** 1178–81
- [3] Fujimoto J G, Brezinski M E, Tearney G J, Boppart S A, Bouma B, Hee M R, Southern J F and Swanson E A 1995 Optical biopsy and imaging using optical coherence tomography *Nature Med.* **1** 970–2
- [4] Srinivasan V J, Huber R, Gorczynska I and Fujimoto J G 2007 High-speed, high-resolution optical coherence tomography retinal imaging with a frequency-swept laser at 850 nm *Opt. Lett.* **32** 361–3
- [5] Hiratsuka H, Morisak K and Yoshimur T 2000 Optical coherence tomography system based on synthesis of optical coherence function with a wavelength-scanning laser source *Opt. Rev.* **7** 442–7
- [6] He Z and Hotate K 1999 Synthesized optical coherence tomography for imaging of scattering objects by use of a stepwise frequency-modulated tunable laser diode *Opt. Lett.* **24** 1502–4
- [7] Yamamoto A, Kuo C, Sunouchi K, Wada S, Yamaguchi I and Tashiro H 2001 Surface shape measurement by wavelength scanning interferometry using an electronically tuned Ti:sapphire laser *Opt. Rev.* **8** 59–63
- [8] Yamaguchi I, Yamamoto A and Yano M 2000 Surface topography by wavelength scanning interferometry *Opt. Eng.* **39** 40–6
- [9] Ansari Z *et al* 2002 Wide-field, real time depth-resolved imaging using structured illumination with photorefractive holography *Appl. Phys. Lett.* **81** 2148–50
- [10] Gabor D 1971 Holography *Nobel Lecture* http://nobelprize.org/nobel_prizes/physics/laureates/1971/gabor-lecture.pdf
- [11] Goodman J W and Lawrence R W 1967 Digital image formation from electronically detected holograms *Appl. Phys. Lett.* **11** 77–9
- [12] Schnars U 1994 Direct phase determination in hologram interferometry with use of digitally recorded holograms *J. Opt. Soc. Am. A* **11** 2011–5
- [13] Schnars U and Jüptner W 1994 Direct recording of holograms by a CCD-target and numerical reconstruction *Appl. Opt.* **33** 179–81
- [14] Schnars U and Jüptner W 2002 Digital recording and numerical reconstruction of holograms *Meas. Sci. Technol.* **13** R85–101
- [15] Yamaguchi I, Kato J, Ohta S and Mizuno J 2001 Image formation in phase-shifting digital holography and applications to microscopy *Appl. Opt.* **40** 6177–86
- [16] Yamaguchi I and Zhang T 1997 Phase-shifting digital holography *Opt. Lett.* **22** 1268–70
- [17] Zhang T and Yamaguchi I 1998 Three-dimensional microscopy with phase-shifting digital holography *Opt. Lett.* **23** 1221–3
- [18] Poon T C 2003 Three-dimensional image processing and optical scanning holography *Advances in Imaging and Electron Physics* vol 126 (Amsterdam: Elsevier) pp 329–50
- [19] Yamaguchi I, Matsumura T and Kato J 2002 Phase-shifting color digital holography *Opt. Lett.* **27** 1108
- [20] Barty A, Nugent K A, Paganin D and Roberts A 1998 Quantitative optical phase microscopy *Opt. Lett.* **23** 817–9
- [21] Cuhe E, Bevilacqua F and Depeursinge C 1999 Digital holography for quantitative phase-contrast imaging *Opt. Lett.* **24** 291–3
- [22] Ferraro P, De Nicola S, Finizio A, Coppola G, Grilli S, Magro C and Pierattini G 2003 Compensation of the inherent wave front curvature in digital holographic coherent microscopy for quantitative phase-contrast imaging *Appl. Opt.* **42** 1938–46
- [23] Xu M L, Peng X, Miao J and Asundi A 2001 Studies of digital microscopic holography with applications to microstructure testing *Appl. Opt.* **40** 5046–51
- [24] Pedrini G and Tiziani H J 1997 Quantitative evaluation of two-dimensional dynamic deformations using digital holography *Opt. Laser Technol.* **29** 249–56
- [25] Picart P, Leval J, Mounier D and Gougeon S 2005 Some opportunities for vibration analysis with time averaging in digital Fresnel holography *Appl. Opt.* **44** 337–43
- [26] Haddad W S, Cullen D, Solem J C, Longworth J W, McPherson A, Boyer K and Rhodes C K 1992 Fourier-transform holographic microscope *Appl. Opt.* **31** 4973–8
- [27] Xu W, Jericho M H, Meinertzhagen I A and Kreuzer H J 2001 Digital in-line holography for biological applications *Proc. Natl Acad. Sci. USA* **98** 11301–5
- [28] Kim M K 1999 Wavelength scanning digital interference holography for optical section imaging *Opt. Lett.* **24** 1693–5
- [29] Kim M K 2000 Tomographic three-dimensional imaging of a biological specimen using wavelength-scanning digital interference holography *Opt. Express* **7** 305–10
- [30] Dakoff A, Gass J and Kim M K 2003 Microscopic three-dimensional imaging by digital interference holography *J. Electr. Imag.* **12** 643–7
- [31] Yu L and Myung M K 2005 Wavelength scanning digital interference holography for variable tomographic scanning *Opt. Express* **13** 5621–7
- [32] Yu L and Myung M K 2005 Wavelength-scanning digital interference holography for tomographic 3D imaging using the angular spectrum method *Opt. Lett.* **30** 2092
- [33] Kim M K, Yu L and Mann C J 2006 Interference techniques in digital holography *J. Opt. A: Pure Appl. Opt.* **8** 512–23
- [34] Gass J, Dakoff A and Kim M K 2003 Phase imaging without 2- π ambiguity by multiwavelength digital holography *Opt. Lett.* **28** 1141–3
- [35] Mann C J, Yu L, Lo C M and Kim M K 2005 High-resolution quantitative phase-contrast microscopy by digital holography *Opt. Express* **13** 8693–8
- [36] Parshall D and Kim M K 2006 Digital holographic microscopy with dual wavelength phase unwrapping *Appl. Opt.* **45** 451–9
- [37] Mann C, Yu L and Kim M K 2006 Movies of cellular and sub-cellular motion by digital holographic microscopy *Biomed. Eng. Online* **5** 21
- [38] Massatsch P, Charrière F, Cuhe E, Marquet P and Depeursinge C D 2005 Time-domain optical coherence tomography with digital holographic microscopy *Appl. Opt.* **44** 1806–12
- [39] Sarunic M V, Weinberg S and Izatt J A 2006 Full-field swept-source phase microscopy *Opt. Lett.* **30** 1462–4
- [40] Yu L and Chen Z 2007 Digital holographic tomography based on spectral interferometry *Opt. Lett.* **32** 3005–7
- [41] Ellerbee A K, Creazzo T L and Izatt J A 2006 Investigating nanoscale cellular dynamics with cross-sectional spectral domain phase microscopy *Opt. Express* **15** 8115–24
- [42] Yu L and Chen Z 2007 Improved tomographic imaging of wavelength scanning digital holographic microscopy by use of digital spectral shaping *Opt. Express* **15** 878–86
- [43] Montfort F, Colomb T, Charrière F, Kühn J, Marquet P, Cuhe E, Herminjard S and Depeursinge C 2006 Submicrometer optical tomography by multiple-wavelength digital holographic microscopy *Appl. Opt.* **45** 8209–17
- [44] Meneses-Fabian C, Rodriguez-Zurita G and Arrizn V 2006 Optical tomography of trans-parent objects with phase-shifting interferometry and stepwise-shifted Ronchi ruling *J. Opt. Soc. Am. A* **23** 298–305

- [45] Gorski W 2006 Tomographic microinterferometry of optical fibers *Opt. Eng.* **45** 125002
- [46] Charrière F, Pavillon N, Colomb T, Heger T, Mitchell E, Marquet P, Rappaz B and Depeursinge G 2006 Living specimen tomography by digital holographic microscopy: morphometry of testate amoeba *Opt. Express* **14** 7005–13
- [47] Charrière F, Marian A, Montfort F, Kühn J, Colomb T, Cuhe E, Marquet P and Depeursinge C 2006 Cell refractive index tomography by digital holographic microscopy *Opt. Lett.* **31** 178–80
- [48] Vishnyakov G N, Levin G G, Minaev V L, Pickalov V V and Likhachev A V 2004 Tomographic interference microscopy of living cells *Microscopy Anal.* **18** 15–7
- [49] Choi W, Fang-Yen C, Badizadegan K, Oh S, Lue N, Dasari R R and Feld M S 2007 Tomographic phase microscopy *Nature Methods* **4** 717–9